Sustainable Cities and Society 131 (2025) 106779

Contents lists available at ScienceDirect

Sustainable Cities and Society

journal homepage: www.elsevier.com/locate/scs

Irregular anisotropy in surface urban heat island footprint

Xinyue Yang [a], Yongze Song [a,*], Cheolhee Yoo [b], Kai Ren [a,c], Peng Wu [a]

[a] School of Design and the Built Environment, Curtin University, Perth, Australia
[b] Department of Land Surveying and Geo-Informatics, The Hong Kong Polytechnic University, Hung Hom, Hong Kong
[c] College of Natural Resources and Environment, Northwest A&F University, Yangling, China

ARTICLE INFO

Keywords:
Surface urban heat island
Spatial heterogeneity
SUHI footprint extraction

ABSTRACT

Footprint and intensity are key indicators for quantitatively analyzing the characteristics of the surface urban heat island (SUHI) effect. Currently, methods based on angle-segmentation and anisotropy have been developed to estimate footprints, but are still greatly challenged by spatial heterogeneity, especially for directional difference. This study develops an adaptive irregular anisotropy (AIA) model to explore the irregular anisotropy in the SUHI effect. The developed AIA model is used to assess the SUHI effect in Sydney, Melbourne, Brisbane, Perth, and Adelaide, Australia. The model dynamically adjusts sector divisions based on the q value to maximize temperature differences between sectors. The results show that the AIA model demonstrates reliable directional adaptability. The SUHI footprint ratio extracted by the AIA model generally ranges from 0 to 8 times the urban area, especially in regions dominated by artificial surfaces or natural bare land. The AIA model also reduces the mean bias in SUHI intensity estimates. Furthermore, the AIA model improves the q value by 1.1 % to 44.1 % compared with existing anisotropy-based extraction models. In summary, this study provides an adaptive SUHI effect estimation method to facilitate the development of SUHI mitigation strategies.

1. Introduction

Urban Heat Island (UHI) refers to the phenomenon where urban temperatures are significantly higher than those in surrounding rural areas (Voogt and Oke 2003), and it has become one of the most obvious environmental issues in the process of urbanization (An et al. 2025; Huang et al. 2024; Shi et al. 2021; Taha 1997). The research on UHI can be divided into two categories: atmospheric UHI (AUHI) and surface UHI (SUHI) (Estoque et al. 2017). AUHI is based on air temperature measurements from meteorological stations (Schwarz et al. 2012; Zhou et al. 2023), whereas SUHI is derived from land surface temperature (LST) observations via remote sensing (Hu et al. 2019; Renard et al. 2019; Sharmin et al. 2024). Due to the limited spatial coverage of meteorological stations, it has failed to effectively characterize the variations in the temperature difference between urban and rural areas (Hu and Brunsell 2015). Therefore, the spatial heterogeneity of land use patterns observed through remote sensing has made SUHI a main topic in UHI research (Das et al. 2020; Tao et al. 2021).

Understanding the formation mechanisms of the SUHI effect is crucial for developing effective mitigation strategies. Numerous studies have shown that urban morphology and spatial factors influence heat storage, surface energy balance, and airflow, thereby shaping the multi-scale spatial variability and temporal evolution of SUHI through nonlinear processes and complex interactions (Guo et al. 2020b; Hou et al. 2023b; Huang and Wang 2019; Liu et al. 2021b; Xu et al. 2024a). At different spatial scales, the contributions of two-dimensional and three-dimensional morphological parameters to SUHI differ significantly (Guo et al. 2020a; Liu et al. 2024; Shao et al. 2023). Among various analytical approaches, the geographically weighted regression (GWR) model has been widely applied to investigate SUHI driving factors at the block, community, and urban functional zone levels (Gao et al. 2022; Yelixiati et al. 2024), as it effectively captures the spatial non-stationarity of variable relationships and enhances the explanatory power for local temperature variation mechanisms (Shi et al. 2025). Furthermore, as an important natural regulatory element, the cooling effect of green spaces is affected by their internal vegetation structure and the layout of surrounding impervious surfaces, which affects the urban thermal environment through cumulative cooling contributions (Gao et al. 2023; Marando et al. 2022). The combined effects of urban morphology, spatial configuration, and ecological components lead to regional differences in the SUHI effect (Peng et al. 2016).

With a deeper understanding of the SUHI effect, effectively

* Corresponding author.
E-mail address: yongze.song@curtin.edu.cn (Y. Song).

https://doi.org/10.1016/j.scs.2025.106779
Received 3 June 2025; Received in revised form 5 August 2025; Accepted 29 August 2025
Available online 30 August 2025

quantifying its spatial characteristics has become a significant challenge. Previous studies have presented the spatial characteristics of the urban thermal environment by performing spatial statistics on LST pixel values within specific regions (Hu and Brunsell 2013). Based on this, researchers have further developed SUHI intensity and footprint to quantify the temperature gradient between urban and suburban areas (Alqasemi et al. 2021; Kim and Brown 2021) and the spatial extent affected by SUHI (Anniballe and Bonafoni 2015; Qiao et al. 2019; Zhou et al. 2015b), respectively. Currently, the quantification of SUHI intensity mainly focuses on defining the reference boundary. For example, Chakraborty et al. (2020) defined SUHI by simplifying urban boundaries and analyzed SUHI patterns and related uncertainties in U.S. urban areas (Chakraborty et al. 2020). In terms of extracting the SUHI footprint, many studies have applied mathematical models to reduce the bias caused by manually setting reference temperatures. For example, Quan et al. (2014) used a Gaussian volume model and MODIS/LST data to analyze the spatiotemporal variation of the SUHI footprint centroid in Beijing (Quan et al. 2014); Qiao et al. (2019) applied a logistic model to automatically identify the summer footprint boundaries in Beijing from 2004 to 2018 (Qiao et al. 2019); Yao et al. (2021) used a Gaussian model to study the spatiotemporal changes of Beijing's footprint and revealed that its expansion trends were significantly correlated with GDP, population, and built-up area growth (Yao et al. 2021). Furthermore, to extract both SUHI intensity and footprint simultaneously, Yang et al. (2023) introduced an adaptive synchronous extraction method, which can automatically identify the optimal background reference area while extracting both intensity and footprint (Yang et al. 2023b). Zhang and Xia (2024) proposed a two-step estimation method to quantify intensity and footprint for 283 cities in China from 2005 to 2019 (Zhang and Xia 2024). Yu et al. (2024) adopted an exponential fitting to quantify the footprint in the Beijing-Tianjin-Hebei urban agglomeration. They identified the inflection point at 95 % of the SUHI impact range as the footprint boundary (Yu and Sun 2024). These methods show certain applicability in addressing the spatial heterogeneity of the SUHI effect.

The three-dimensional structure of the urban surface leads to directional differences in solar radiation reception, which in turn results in directional characteristics in LST observed via remote sensing (Ermida et al. 2017; Hu et al. 2016; Hu and Wendel 2019; Qin et al. 2023). However, most existing estimation methods assume isotropic spatial expansion. This assumption may introduce bias in the estimation of the SUHI footprint and intensity. For example, multi-ring buffer analysis may cover mixed land use types, which may affect the definition of the background area. (Wang et al. 2024). Similarly, although the Gaussian model is less sensitive to background area definitions and avoids subjective bias (Kumar et al. 2023; Li et al. 2022), it performs poorly in cities with irregular shapes or complex terrain (Rehman et al. 2021; Yang et al. 2019). In addition, Wu et al. (2024) showed that due to heterogeneity within oases, LST shows opposite trend changes in certain directions, affecting the accuracy of the fitted curve (Wu and Chen 2024).

To address this issue, some studies have proposed angle-based segmentation approaches to capture the spatial heterogeneity of SUHI in different directions. For example, Yang et al. (2023) proposed an anisotropy hypothesis-based method, which combines angle segmentation with an exponential decay model to improve the accuracy of SUHI footprint estimation (Yang et al. 2023a). Similarly, Xu et al. (2024) applied a 5-degree interval segmentation combined with a logistic model to analyze the spatiotemporal characteristics of SUHI footprints (Xu et al. 2024b). These methods improve the accuracy of footprint estimation to a certain extent by considering the directional expansion characteristics of SUHI. However, these anisotropic methods still face significant challenges. Urban expansion is often uneven (Jiao et al. 2021; Zhong et al. 2022), with different development patterns in different directions (Simwanda et al. 2019; Xu et al. 2024b; Yang et al. 2024). Therefore, it is important to account for directional differences in LST caused by the surrounding landscape when estimating the SUHI footprint.

To sum up, this study develops an Adaptive Irregular Anisotropy (AIA) model to characterize the SUHI footprint and intensity anisotropy. The q-value represents the degree of temperature distribution dispersion within each sector and is used to quantify the spatial heterogeneity of temperature gradients. By maximizing the q-value, the model adaptively optimizes sector divisions, thereby effectively capturing the directional variation pattern of SUHI effects. This method addresses the limitations of isotropic and regular anisotropic methods in directional assumptions to some extent, providing a more reliable analytical framework for evaluating SUHI patterns across different cities.

2. Study area and datasets

This study used Landsat-8 data from 2018 provided by Google Earth Engine (GEE) to retrieve LST and characterize the SUHI effect. The AIA model, proposed based on the spatial heterogeneity of LST, divides and merges regions according to temperature variations in different directions. The model extracts the mean LST from the intersections of regions and buffer zones and applies temperature decay curves to fit the mean temperature, thereby simultaneously assessing intensity and footprint. The following sections will detail the construction of this framework and its application in analyzing the anisotropic patterns of the SUHI effect in five representative Australian cities.

2.1. Study area

Australia is the largest country in Oceania, with a unique geographical location and complex urban development patterns (Eliades et al. 2024; Harmay et al. 2021). This study focuses on five major cities, including Sydney, Melbourne, Brisbane, Perth, and Adelaide. Sydney and Brisbane are located in the humid subtropical climate zone, Melbourne and Adelaide are in the oceanic climate zone, and Perth is in the Mediterranean climate zone. These cities have high vegetation coverage and are distributed along the coastline (Calderón-Loor et al. 2021; Gao et al. 2024). Such factors influence the intensity and extent of the SUHI effect, as large areas of greenery help alleviate heat accumulation. At the same time, coastal characteristics affect temperature distribution through sea breezes and humidity. However, current research on the SUHI effect in Oceania is relatively limited, particularly regarding the heterogeneous expansion of the SUHI effect (Fig. 1).

2.2. Data preparation

Surface temperature observations were obtained from the Landsat-8 satellite through the Statistical Mono-Window (SWM) algorithm provided by Ermida et al.(2020) (Ermida et al. 2020). The LST maps retrieved by the SMW algorithm have been shown to posses a satisfactory accuracy (Ermida et al. 2020; Li et al. 2023; Naserikia et al. 2023). They were averaged lst observations with December to February and June to August for summer and winter, respectively. To ensure data quality, only daytime scenes with less than 10 % cloud cover were used (Kafy et al. 2023; Unal Cilek and Cilek 2021). The study used the 30-meter resolution Copernicus Digital Elevation Model GLO-30 and the global water dataset provided by the Joint Research Centre to remove the influence of terrain and water bodies on the LST data. Land cover data were sourced from the 2018 Digital Earth Australia (DEA) Land Cover dataset, which provides a detailed surface classification system, including various types of vegetation (e.g., cultivated and natural vegetation) and surface types (e.g., artificial surfaces and natural bare ground). Administrative boundaries were obtained from the Statistical Area Level 1 data provided by the Australian Bureau of Statistics (ABS) for Local Government Areas (LGAs), and population data from ABS were used to calculate the centroids of built-up areas. As the core of the urban-rural temperature gradient, the built-up area data is sourced from the global urban boundary dataset (GUB) (Li et al. 2020), which is based

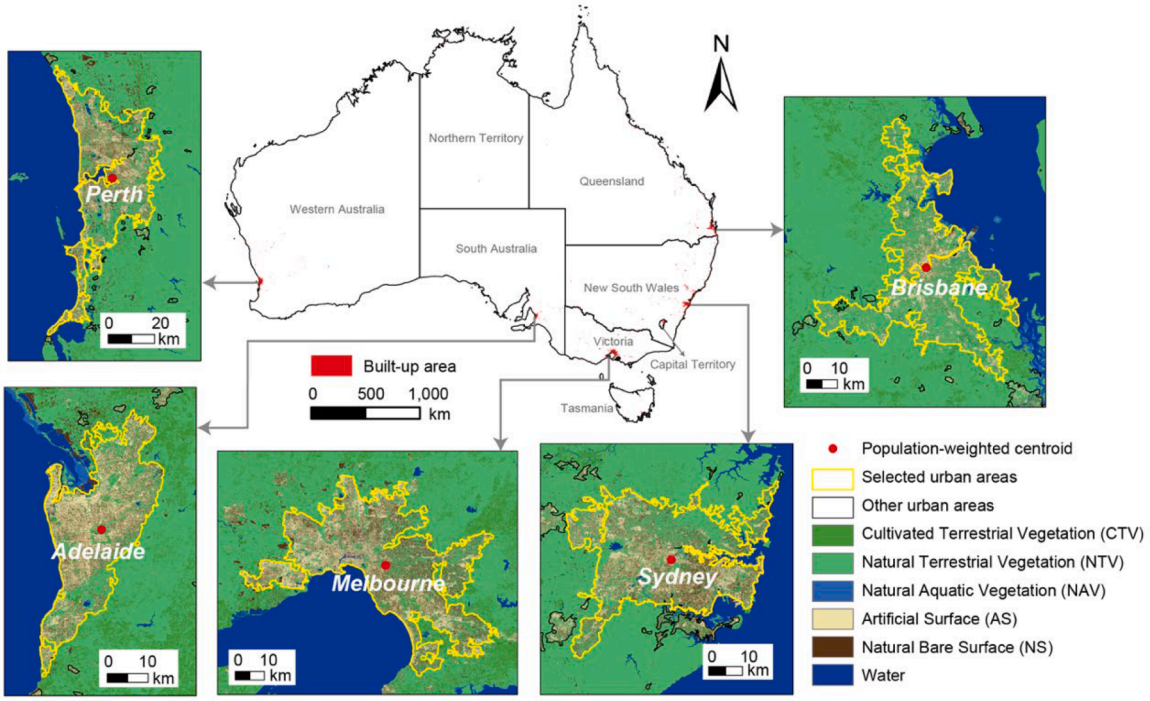

Fig. 1. Study area. The population-weighted data is calculated by using the centroid coordinates of each LGA from ABS, with the total population of each LGA as the weight for its centroid, to determine the centroid of the entire selected built-up area.

on Global Artificial Impervious Area data and generated using kernel density estimation and cellular automata models on the GEE platform, covering multiple periods from 1990 to 2018. The coastline data was obtained from the OSMCoast500 dataset provided by Australia's Commonwealth Scientific and Industrial Research Organisation (CSIRO). This dataset is based on the global high-precision land boundary data provided by OpenStreetMap (OSM) and has been simplified for use in locating the source of the cooling effect from the ocean.To ensure accuracy in data analysis, all datasets were resampled to match the resolution of the LST data to avoid uncertainties or biases due to resolution differences.

2.3. Estimation of SUHI footprint

2.3.1. LST retrieval

The Statistical Mono-Window algorithm (Duguay-Tetzlaff et al. 2015; Nadizadeh Shorabeh and Hamzeh 2019) for extracting LST from Landsat-8 data uses an empirical relationship between top-of-atmosphere (TOA) brightness temperature and LST. First, the TOA brightness temperature (Tb) is obtained from the thermal infrared band and then corrected based on surface emissivity (ε). The specific formula is as follows:

$$LST = A_i\frac{Tb}{\varepsilon} + B_i\frac{1}{\varepsilon} + C_i \quad (1)$$

where, A_i, B_i, C_i are coefficients derived from radiative transfer simulations using linear regression. These simulations are conducted for 10 different classes of total column water vapor (TCWV) ($i = 1, \ldots, 10$).

2.3.2. Adaptive irregular anisotropy model

The specific process of the AIA model is illustrated in Fig. 2. First, multiple equal-area buffer zones are generated. Then, LST pixels affected by terrain and water bodies are removed. Equal-angle sectors are created from the centroid of the built-up area and intersected with the buffer zones. Each iteration optimises the sector division by adjusting parameters such as sector angle and temperature threshold to maximize the q-value. An exponential decay function is then applied to fit the temperature data in each sector, and curvature is calculated to identify key inflection points along the fitted curve, which are used to extract SUHI intensity and footprint. Sectors that cannot be fitted with the exponential decay curve or are significantly affected by water bodies are excluded from the analysis..

(1) Constructing multiple equal-area buffers

The built-up areas of five study areas were extracted from the GUB dataset and processed using morphological operations for expansion and contraction. Although some impervious surfaces such as small towns and rural settlements exist within the buffer zones, they were not considered in this study because their built-up areas are all below 50 km^2 and have a limited thermal impact on the SUHI effect in the main study areas (Yang et al. 2023b). Then, starting from the boundary of the built-up area, 20 concentric buffer zones were generated outward by iteratively increasing the buffer distance, such that each ring had an equal area increment equivalent to 50 % of the built-up area. In total, the buffer zones covered an area 11 times larger than the built-up area. Based on the previous findings (Yang et al. 2023b; Zhou et al. 2014), we assume that the SUHI footprint is located within these buffer zones.

(2) Removing regions influenced by local temperature disturbances

Before quantifying the SUHI footprint, a two-step filtering process was applied to the LST dataset. First, the average elevation (EAve) of the central urban area was calculated using the SRTM DEM, and all pixels with elevation values outside the range of EAve ± elevation threshold (Et) were excluded. This relative threshold maintains consistency in temperature anomaly filtering. Therefore, the same Et was applied uniformly across all five cities and was typically set to 50 m (Imhoff et al. 2010; Yang et al. 2023b). In addition, permanent water bodies were masked using the JRC Global Surface Water dataset to eliminate the influence of aquatic surfaces on LST. After these filtering steps, the remaining pixels were used for subsequent sector division to

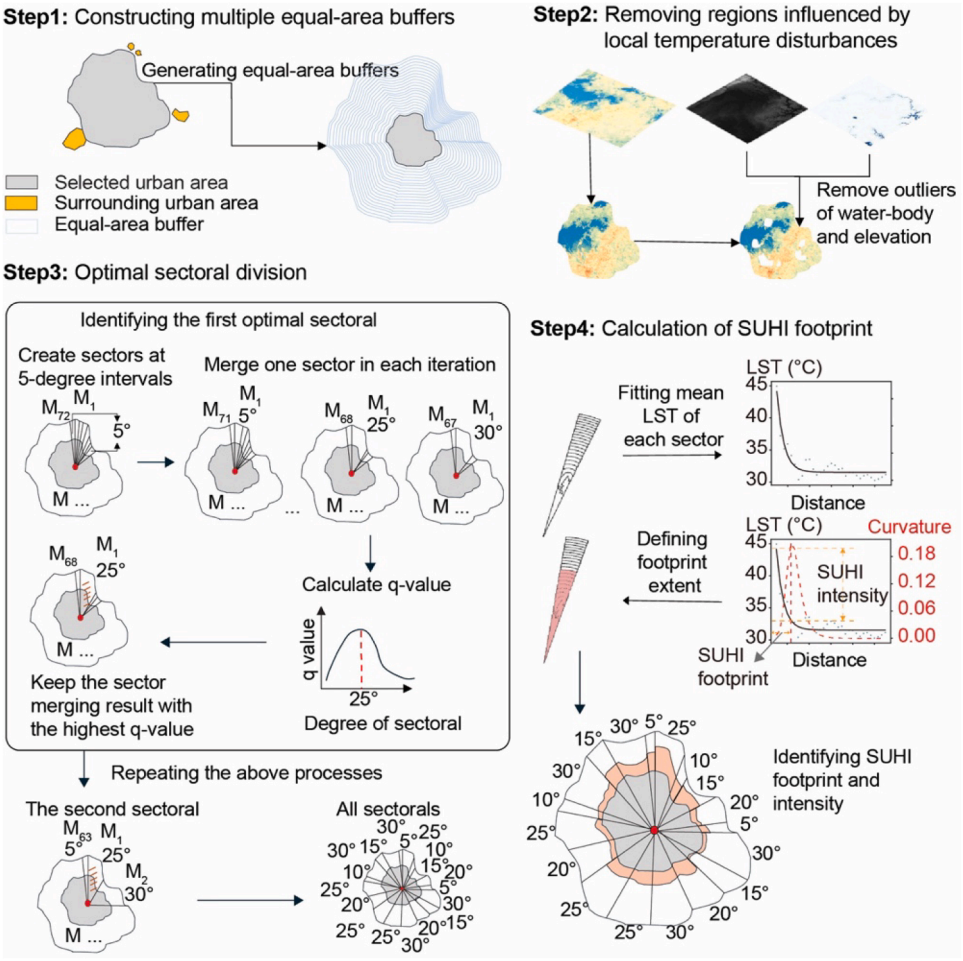

Fig. 2. Workflow of the AIA model for extracting SUHI footprint and intensity.

reduce the impact of local temperature anomalies on the temperature fitting curve.

(3) Optimal sector division

The q value is an indicator used to measure the degree of spatial heterogeneity (Song et al. 2020; Song and Wu 2021), calculated by comparing the variance within each sector to the overall regional variance. It reflects the extent to which the sector structure explains the spatial variability of temperature. A higher q value indicates more significant temperature differences between sectors and a more reasonable spatial stratification.

The AIA model begins at the population-weighted centroid, and to ensure a sufficient number of LST observations and reduce the influence of local anomalies, the buffer is divided into multiple sectors at 5-degree intervals. The LST of each sector is then calculated, and a temperature threshold is applied to determine whether adjacent sectors should be merged or retained. This merging process is performed iteratively, recalculating the q value at each step. If the q value increases after merging, it indicates enhanced spatial heterogeneity and the merger is accepted; otherwise, the original division is retained. Compared with fixed-angle division methods, the q value provides a quantitative basis for optimizing sector boundaries, enabling the effective extraction of the directional and irregular expansion patterns of the SUHI footprint. The calculation formula for the q value is as follows (Wang et al. 2016):

$$q = 1 - \frac{\sum_{i=1}^{k} N_i \sigma_i^2}{N_{total} \sigma_{overall}^2} \tag{2}$$

where k represents the number of sectors, N_i represents the number of LST points in the i th sector, σ_i^2 represents the variance within the i th sector, N_{total} represents the total number of data points in the entire study area, $\sigma_{overall}^2$ represents the overall variance of the entire study area.

(4) Calculation of SUHI footprint

From the city centre outward, the surface temperature usually decreases with increasing distance and shows a decay trend at a decreasing rate. The exponential decay function can better describe this temperature-distance relationship, and its parameters have clear physical significance (Li et al. 2017; Tao et al. 2021; Wang et al. 2025; Yang et al. 2022). These parameters can be used to analyze the intensity and footprint of the SUHI effect, and the fitting performance of the function has been validated in previous studies (Zhang and Xia 2024; Zhou et al. 2015a). In addition, the function is less sensitive to local temperature anomalies and can accurately identify the turning point of temperature change.

The reference LST threshold is determined by calculating the curvature within a local window, where the turning point (TP) with the maximum absolute curvature corresponds to the LST of the reference area.

$$T(d) = A \cdot e^{-\frac{d}{t}} + T_0 \tag{3}$$

$$k = \frac{\ddot{y}}{(1+\dot{y}^2)^{\frac{3}{2}}} \quad (4)$$

where T_d is the fitted temperature at a given distance d.; T_0 is the background or baseline temperature; t is the decay time constant or scale parameter; k is the curvature of the temperature decay curve, where $\ddot{y}$ is the second derivative of the curve and $\dot{y}$ is the first derivative of the curve. When k is maximum, the buffer with d less than this value is the SUHI footprint; A represents the initial amplitude or coefficient of decay. In this context, when the value of A is greater than zero, it is referred to as SUHI intensity, while negative values are referred to as the surface urban cool island (SUCI) intensity.

2.4. Model validation

2.4.1. Model performance

Since this study mainly considers the spatial heterogeneity of SUHI effects, an equal-angle sector division method is used for method comparison. The effectiveness of these methods will be evaluated based on the q-value to determine which approach maximizes LST heterogeneity. In addition, differences in the ability of each method to extract SUHI intensity and SUHI footprint will be analyzed.

2.4.2. T-test for assessing the significance of heterogeneity between sectors

Since the method proposed in this study is based on the assumption of anisotropy in LST distribution, a *t*-test is used to verify the reliability of the method by comparing the t-values between the optimal sector division and the equidistant division. The *t*-test is applied to compare the differences in LST values between adjacent sectors (Voelkel et al. 2018). The formula for the *t*-test is:

$$t = \frac{\overline{X}_1 - \overline{X}_2}{\sqrt{\frac{s_1^2}{n_1} + \frac{s_2^2}{n_2}}} \quad (5)$$

where $\overline{X}_1$ and $\overline{X}_2$ are the sample means of the two sectors being compared; s_1^2 and s_2^2 are the sample variances of the two sectors; n_1 and n_2 are the sample sizes of the two sectors.

2.4.3. Sensitivity to parameters

As shown in Table 1, the methodology in this study mainly involves four parameters: buffer size, min and max sector angles, and temperature threshold. The first three parameters define the spatial structure of the analysis, while the temperature threshold dictates how temperature variations are segmented and analysed. During the sensitivity tests, only one parameter is changed at a time, with the others held at their default values.

Table 1
Parameters and their values in the AIA model.

Parameters	Descriptions	Default values	Values for sensitivity tests
$Buffer_{size}$	The ratio of the size of each buffer to the size of the central urban area	1/2	½, ¼, 1/5, 1/8, 1/10
Min sector angle	The minimum angle for sector division	5	1,2,3,5
Max sector angle	The maximum angle for sector division.	30	20,25,30
Temperature Threshold	The minimum temperature difference used to merge sectors	0.1	0.05,0.1,0.15,0.2,0.25

3. Results

3.1. Optimal sector division based on temperature variations

Fig. 3 shows the process of quantifying SUHI effects using a single sector as an example. In Figs. 3b and 3f, we observe that the point of maximum curvature can effectively identify the turning point of the temperature decay curve, though sometimes this curvature peak may appear before the actual turning point. This disparity appearsbecause curvature captures the intensity of geometric changes in temperature decay, while the turning point is associated with the underlying physical process of temperature variation. Figs. 3c and 3g further show the distribution characteristics of turning points and the variability in temperature decay: in summer, turning points are more dispersed, while in winter, they cluster more tightly. Specifically, Perth's turning points appear within a range of 1 to 3 times the urban area, whereas, for the other four cities, turning points can extend up to 7.5 times the urban area. In Figs. 3d and 3h, we see that beyond a distance of about one urban area, Perth shows the most consistent frequency of turning points across directions in both summer and winter, approximately 15 % and 20 %, respectively, indicating minimal variation in expansion distances across directions. Melbourne, however, displays the farthest-reaching turning points in both seasons, extending over six times the urban area. Overall, temperature decay processes show significant directional variability across different seasons and cities.

3.2. The spatial distribution characteristics of SUHI intensity

Fig. 4 illustrates the distribution of SUHI intensity across different directions in the study areas during summer and winter. In summer, Sydney's SUHI effect is concentrated in the west and northwest, with an intensity of about 4.8 °C and a maximum of 8 °C in the north. Brisbane's SUHI effect is more dispersed, mostly distributed in the west, with a maximum intensity of about 6 °C. Notably, Melbourne, Perth, and Adelaide show both SUHI and SUCI effects in the same direction. Among them, Melbourne's SUHI and SUCI effects in the north show the greatest difference, with an absolute intensity difference of about 5 °C, while Perth's SUHI and SUCI effects in the south are nearly equal, with absolute intensity values both around 6 °C.

In winter, the SUHI effect becomes more concentrated, and its directional pattern differs from that in summer. For example, Sydney's SUHI is concentrated in the southwest, with a maximum SUHI intensity of 9.6 °C, while Adelaide's SUHI is mostly concentrated in the east and southeast, with a maximum SUHI intensity of 5.5 °C. Overall, SUHI intensity varies between different directions, and variations also exist within the same direction, where SUHI and SUCI effects sometimes occur simultaneously.

3.3. The spatial distribution characteristics of SUHI footprint

Fig. 5 presents the extracted SUHI footprint and land use area statistics for five cities. Only sectors with A greater than 0 are used to extract the footprint. Overall, the SUHI footprint range in summer is larger than in winter, showing directional characteristics. For example, in the western direction of Sydney, the footprint extends the furthest, with SUHI effects more concentrated. Besides, directions with concentrated SUHI effects often have a high proportion of Artificial Surface (AS) or Natural Bare Surface (NS) areas, such as the west and north directions in Sydney and the east, north, and northeast directions in Melbourne. In Adelaide, while the AS proportion is lower, the NS proportion is relatively high. In contrast, directions with higher proportions of vegetation types (e.g., Cultivated Terrestrial Vegetation and Natural Terrestrial Vegetation) tend to mitigate the SUHI effects to some extent. For instance, in the north and northeast directions of Perth, vegetation-related land cover reaches 50 %, with both SUHI intensity and SUCI intensity close to 8 °C (Fig. 4).

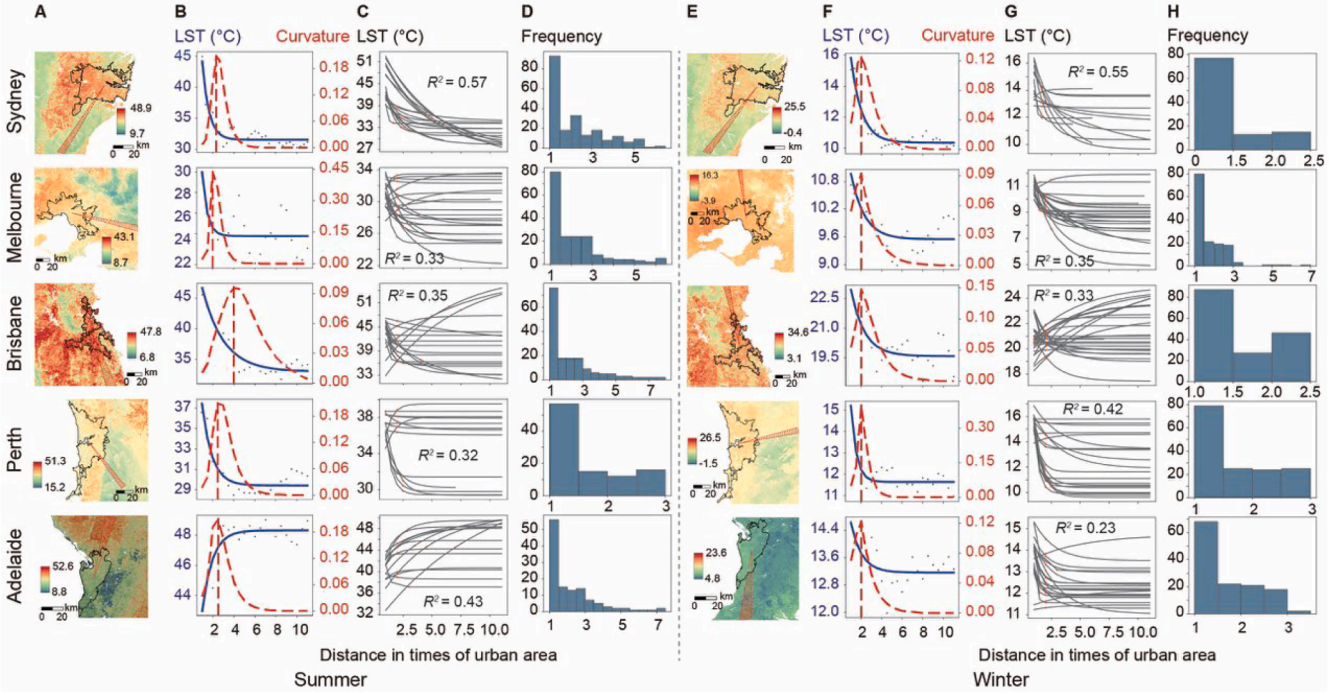

Fig. 3. Sectoral temperature decay curve fitting and curvature-based inflection point extraction with turning point distribution across all sectors. A) and E) the AIA model identifies the position of a specific sector, while B) and F) show the temperature decay curve for that sector. The blue solid line represents the fitted result of the temperature decay curve, and the red dashed line represents the curvature change curve. The intersection of the dashed line with the blue solid line is the turning point, which is used to calculate SUHI intensity and SUHI footprint. C) and D) display the temperature decay curves and its average R^2. G) and H) show the frequency distribution of turning points for all sectors.

To verify the statistical significance of the AIA model, Figs. 6a-6c show the difference in LST means and *t*-test results for a pair of sectors, while Fig. 6d shows the *t*-test results for multiple sectors in the north direction. Figs. 6e and 6f show the proportion of all sector pairs in the five cities that passed the *t*-test. Some sectors did not pass the t-significance test, indicating that not all sectors in the same direction are included in the footprint calculation. In other directions (e.g., northeast and southeast), despite a high proportion of sectors passing the significance test, sectors that cross water bodies or cannot fit the temperature decay curve are excluded from the footprint calculation. Overall, land cover types significantly influence the spatial heterogeneity of SUHI effects, with areas of high AS or NS coverage showing a more concentrated footprint, while areas with more vegetation types tend to mitigate the SUHI effects.

3.4. Model validation

Model uncertainty was addressed through a sensitivity analysis of four key parameters. Specifically, Section 3.4.1 evaluates the sensitivity of the q-value to buffer size, minimum and maximum sector angles, and temperature threshold by changing one parameter at a time while keeping the others constant. Section 3.4.2 further assesses the robustness of the AIA model by comparing the q-values extracted under different equal-angle division models.

3.4.1. Sensitivity analysis of different parameters on q-values

Fig. 7 presents the sensitivity analysis of q values for five cities in both summer and winter across different parameters. Specifically, changes in buffer size and max sector angle have minimal impact on q values for all cities, with q values remaining relatively stable within the range of buffer sizes from 1/2 to 1/10 and max sector angles from 20 to 30 degrees, indicating a low influence of these parameters on temperature heterogeneity. For the min sector angle, q values are mostly stable when changing from 1 to 3 degrees but show a slight decrease at 5 degrees. Since there are fewer data points in each sector, narrower sector divisions may lead to unstable curve fitting, so 5° intervals are selected as the default interval to balance spatial resolution and computational efficiency. In contrast, increasing the temperature threshold leads to a significant rise in q values, particularly in summer; for example, q values for Melbourne, Adelaide, and Sydney increase by more than 0.1 when the temperature threshold exceeds 0.2, reaching over 0.5 for Melbourne and Adelaide and around 0.25 for Sydney, with similar upward trends observed in other cities. This shows that the temperature threshold is a key parameter affecting the accuracy of the AIA model's analysis of the SUHI effect. An appropriate threshold can significantly improve the q value of the sector division, thereby more effectively capturing the spatial heterogeneity of temperature.

3.4.2. Sensitivity analysis of the AIA model

Table 2 shows the improvement in q-values achieved by the AIA model compared to the equal-angle divisions methods. Overall, the AIA model outperforms the equal-angle division methods, significantly improving q values ranging from 1.1 % to 44.1 % across all cities and seasons. This suggests that smaller equal-angle divisions can capture directional temperature characteristics to some extent, but the AIA model is more adaptive in capturing the spatial heterogeneity of temperature. Higher q values indicate greater temperature differences between sectors, showing that heat is more concentrated in specific directions, while lower q values suggest a more even temperature distribution across sectors within a city. Although the overall q values are relatively low, potentially due to the complexity of urban structures and the relatively even SUHI effects in certain cities and seasons, the adaptive division method still significantly enhances the ability to capture the spatial heterogeneity of SUHI effects.

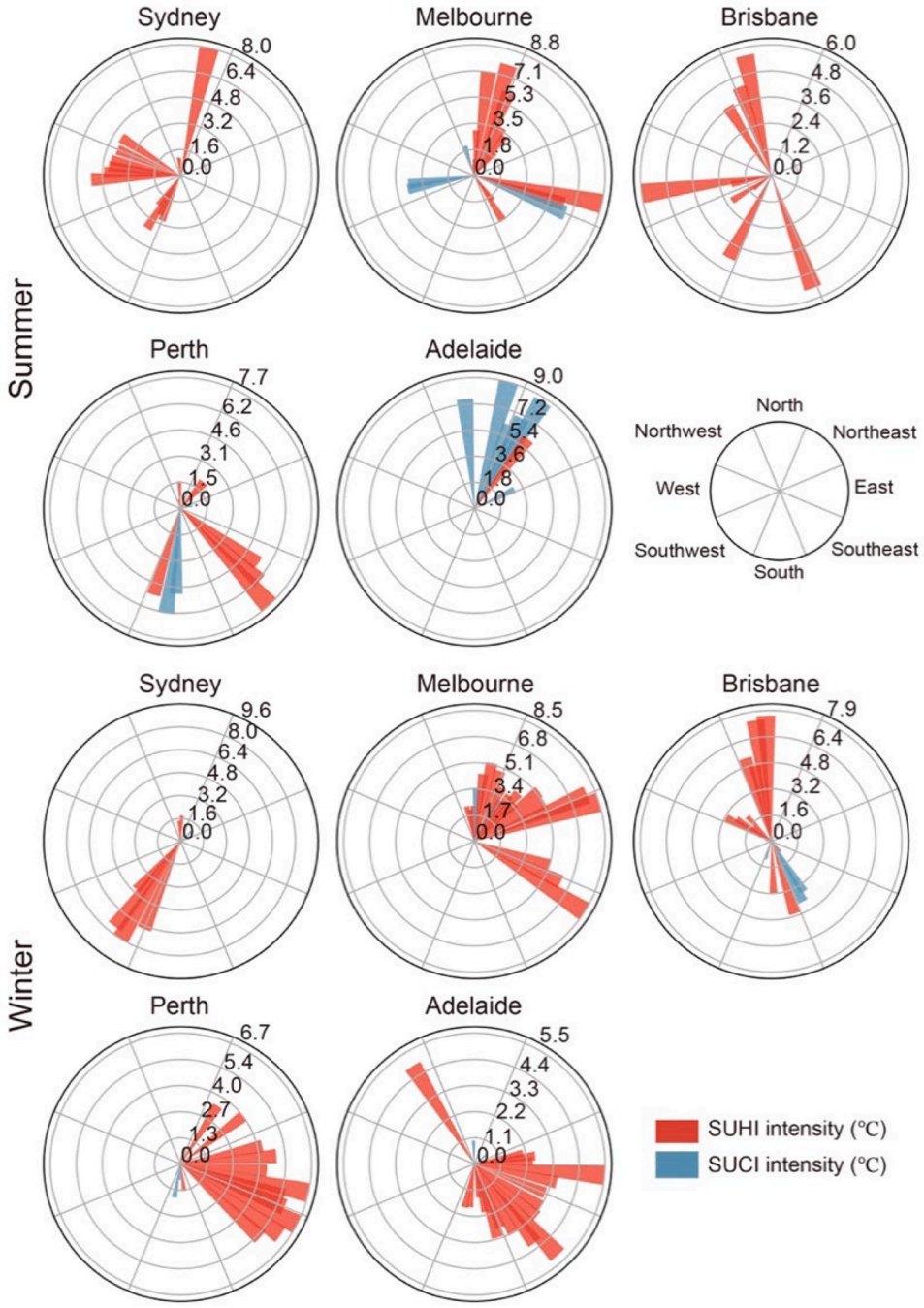

Fig. 4. Spatial differences in SUHI intensity (°C) distribution across eight directional angles. Each direction covers 45 degrees, starting with the north direction, whose angle range is from 337.5 to 22.5 degrees. The remaining directions are divided sequentially in a clockwise manner, with each directional marker pointing to the midpoint of its angle range (for example, the northeast direction has an angle range of 22.5 to 67.5 degrees, with its marker pointing to 45 degrees).

4. Discussions

4.1. Comparison with other methods

Existing studies have widely adopted machine learning (ML) and deep learning (DL) methods to identify the spatial patterns of the SUHI effect (Oh et al. 2020). Among them, interpretable ML models (such as SHAP, LIME) have also been used to quantify the nonlinear interactions between variables and their contributions to the SUHI effect (Hou et al. 2023a; Zhu et al. 2025). These methods can effectively capture complex spatial dependencies and achieve fitting accuracy above 0.95 in multiple studies (Liu et al. 2021a; Oukawa et al. 2022; Tanoori et al. 2024). However, their outputs often lack physical interpretability. Unlike other methods, the main advantage of the AIA model is that it measures temperature differences between adjacent sectors rather than absolute temperature values. This differentiated measurement is relatively independent of land type restrictions, so it is not significantly affected by differences in urban and rural surface coverage.

As shown in Fig. 8, the AIA model overcomes the limitations of equal-angle sector division in extracting SUHI intensity and SUCI intensity. For example, in summer in Sydney, the upper and lower quartiles of A values range from approximately 6.4 °C to 7.5 °C, while Sector-5 and Sector-15 can only extract a limited number of valid A values, and Sector-22.5 cannot extract any valid A values. Additionally, the equal-angle

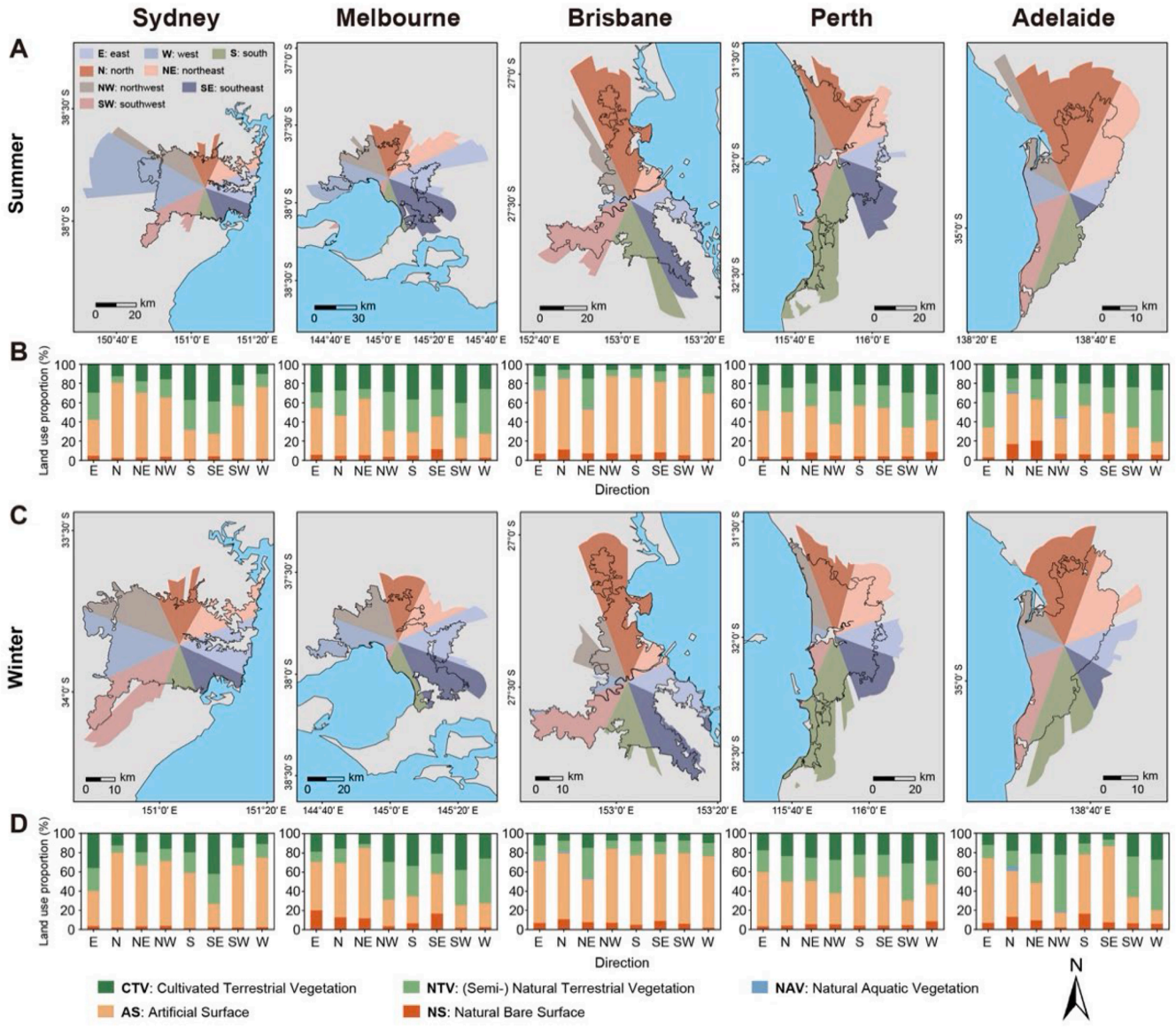

Fig. 5. Spatial distribution of SUHI footprint and land use statistics across directions. A) and C) show the extracted SUHI footprint for summer and winter, respectively. B) and D) show the proportion of land cover types within each sector.

partitioning method overestimates the SUHI intensity to some extent, especially in Brisbane during summer, where the median A value extracted by the equal-angle partitioning method is close to 8 °C, while the AIA model's median is −1.2 °C. This overestimation may occur because the equal-angle division averages the overall temperature difference, including green or cooling areas into high-temperature areas, thus ignoring the contribution of the cold island effect.

Typically, arid areas tend to have negative intensity values because urban areas in these regions have higher vegetation cover, building shading, and smoother aerodynamic structures than surrounding deserts (Dialesandro et al. 2019; Li et al. 2019; Zhou et al. 2014), leading to lower urban surface temperatures. However, the cities in this study are located in coastal areas with humid climates, yet still display low SUHI intensity values. This may be related to the high density of urban green spaces and the cooling effect of water evaporation (Huang and Wang 2019), which contributes to a SUCI effect in specific directions.

Fig. 9 shows the statistical differences between the SUHI footprint extracted by the AIA model and other methods. In summer, Sydney's SUHI effects extend the farthest to the west, with a buffer distance of up to eight times the city area. In winter, Melbourne's SUHI effects extend the farthest, with a stronger SUHI effect on the east side compared to the west, and an extension distance in the southeast direction that can reach six times the city area. The hottest areas in Melbourne in 2018 located in the northwest and southeast regions may be related to the low soil moisture and high impervious surface area in these directions (Jamei et al. 2022). This is consistent with previous studies, which concluded that the SUHI footprint range is usually between 6 and 8 times that of the central urban area (Li et al. 2017; Yang et al. 2023a), with variations between different cities.

In certain directions, SUHI and SUCI effects can coexistence, likely driven by a combination of factors. Australian urban planning achieves a staggered layout of buildings and green spaces through mixed land use (Clay et al. 2016; Herath et al. 2024; Lu et al. 2024). Furthermore, the localized cooling effect of coastal winds can create SUCI effects near the coast, while areas further inland still display the SUHI effect. To quantify the SUHI effect, the AIA model maximizes the temperature difference between sectors using the q value to enhance heterogeneity between sectors and ensure a more homogeneous temperature distribution within them. Unlike previous studies that directly exclude mixed sectors, this model uses a merging strategy to spatially improve

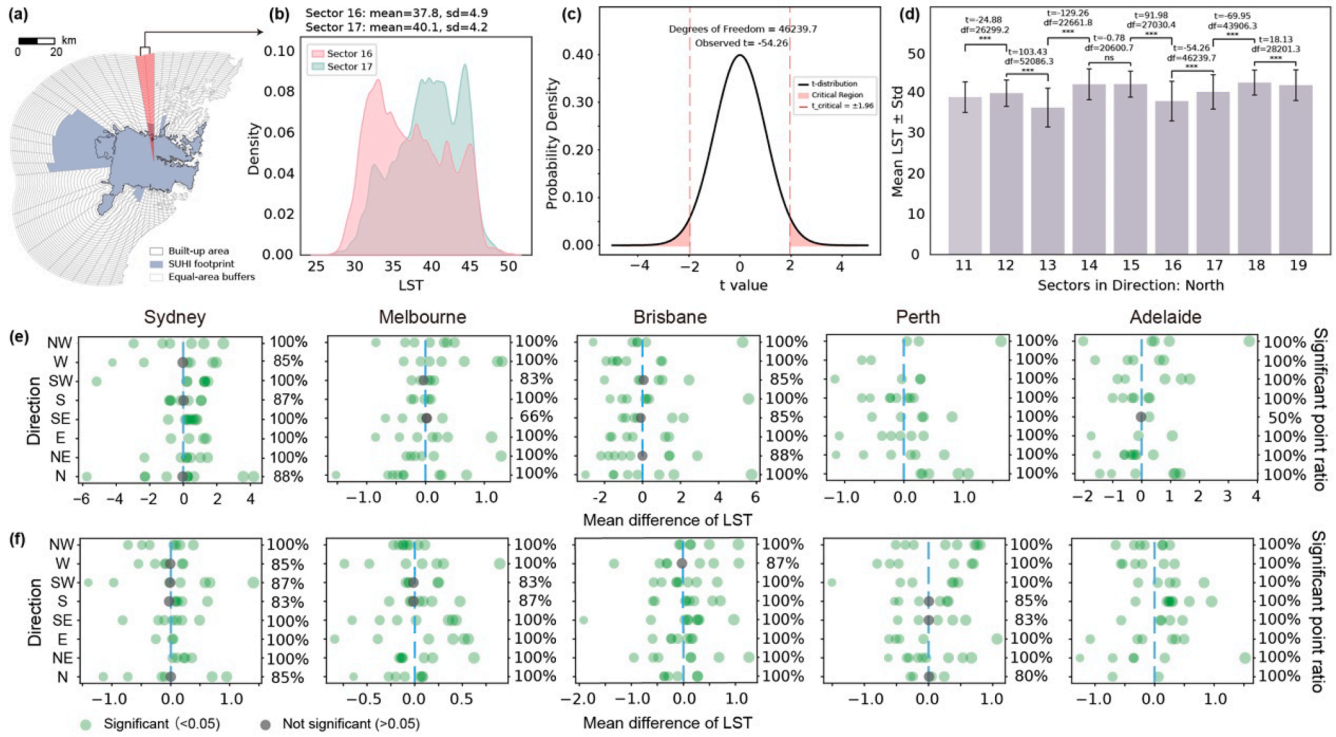

Fig. 6. T-test validation of LST differences between sectors divided by the AIA model. A) shows two sectors (Sector 16 and 17) for example; B) LST distribution curves for two sectors; C) the distribution graph of the two sectors independent sample t-test; D) shows the LST mean values of each sector in the north and the significance test results of their pairwise comparisons. Asterisks indicate different significance levels; E) and F) display the *t*-test results between different sectors, where the x-axis represents the t-value, the left y-axis represents the eight directional angles, and the right y-axis indicates the proportion of sectors in each direction that passed the significance test.

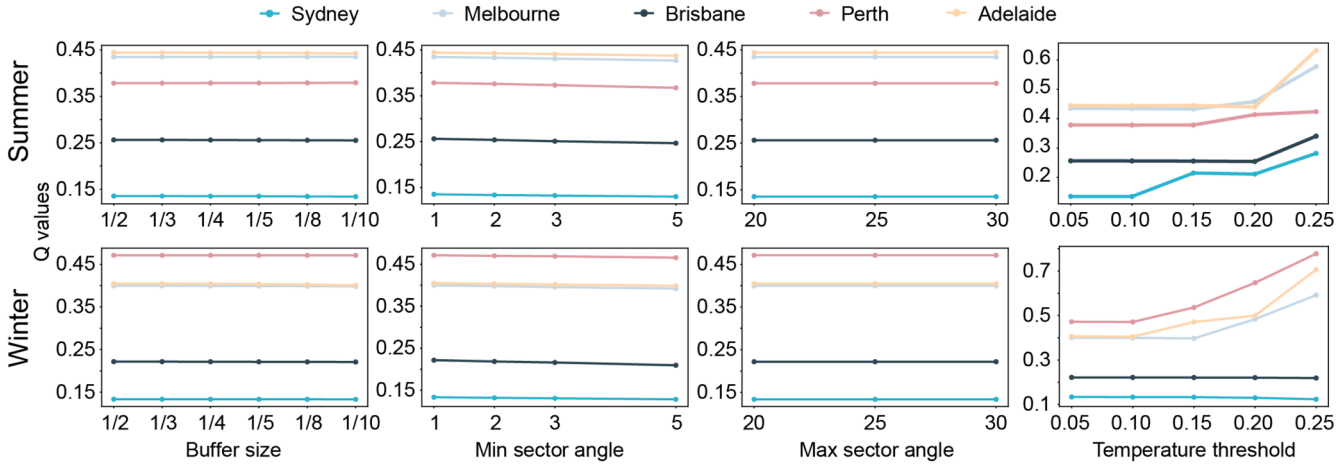

Fig. 7. Sensitivity analysis of q values to AIA model parameters.

temperature zoning. Furthermore, sectors displaying a SUCI effect are not used to calculate the SUHI footprint, further improving identification accuracy.

4.2. Differences in SUHI effects and their causes

Due to the combined effects of geographical conditions, urban morphology, and surrounding land use, the study area shows significant irregular anisotropy in the SUHI footprint. For example, the northern region of Melbourne has relatively uniform land use (Calderón-Loor et al. 2021), resulting in minimal differences in SUHI footprint in these directions, while the western region is a typical agricultural area; the high complexity of the landscape leads to the disappearance of the temperature gradient (Ge et al. 2021), making it difficult to observe effective SUHI effects. Sydney's SUHI effects are mainly influenced by the western and southwestern regions, while the northern and southern regions are less affected. This is because the high building density and impervious surfaces in the western region significantly enhance the SUHI effect, whereas the northern and southern regions, with extensive forest and water body coverage, experience a rapid decrease in LST, thereby inhibiting the expansion of the SUHI effect (Pfautsch et al. 2024). Under low winter wind conditions, inland areas of Adelaide and Perth are more susceptible to higher heat stress (Sharifi et al. 2020). These two cities have distinct topographical features, with hills to the

Table 2
Comparison of q values between the AIA model and equal-angle division methods.

Season	City	Range of merged sector angles	Q value (AIA)	Q value of equal-angle division methods			% Δ vs 22.5°	% Δ vs 15°	% Δ vs 5°
				22.5°	15°	5°			
Summer	Sydeny	[5, 15]	0.1352	0.1086	0.1146	0.1301	24.6 %	18.0 %	3.9 %
	Melbourne	[5, 20]	0.4348	0.3852	0.4011	0.4276	12.9 %	8.4 %	1.7 %
	Brisbane	[5, 15]	0.2563	0.1819	0.2168	0.2468	40.9 %	18.2 %	3.8 %
	Perth	[5, 30]	0.3783	0.2626	0.3144	0.3672	44.1 %	20.3 %	3.0 %
	Adelaide	[5, 30]	0.4443	0.3767	0.3922	0.4011	17.9 %	13.3 %	10.8 %
Winter	Sydeny	[5, 15]	0.1335	0.1081	0.1062	0.1285	23.5 %	25.8 %	3.9 %
	Melbourne	[5, 15]	0.3997	0.3852	0.3748	0.3937	3.8 %	6.7 %	1.5 %
	Brisbane	[5, 15]	0.2217	0.1569	0.1765	0.2096	41.2 %	25.6 %	5.8 %
	Perth	[5, 20]	0.4711	0.4181	0.4455	0.4659	12.7 %	5.8 %	1.1 %
	Adelaide	[5, 25]	0.4048	0.3430	0.3749	0.3991	18.0 %	8.0 %	1.4 %

Note: All q-values were statistically significant at a 95 % confidence level.

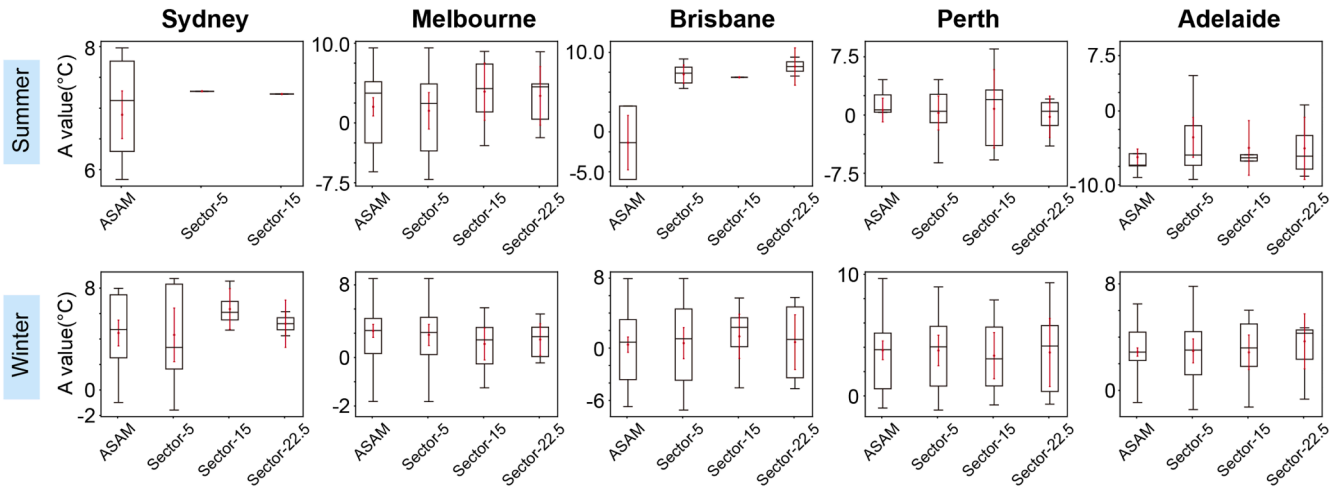

Fig. 8. Comparison of A-Values between AIA model and different equal-angle division methods.

east and the sea to the west. This topographic structure may limit the impact of cold ocean air currents on coastal areas, allowing heat to accumulate more easily inland away from the coast, leading to the inland expansion of the winter SUHI footprint in these two cities.

In general, urban vegetation, the cooling effects of water bodies, ventilation corridors, and building shading can reduce urban LST (Li and Chen 2023; Xie et al. 2024), resulting in low or even negative SUHI intensity, which in turn limits the expansion of the SUHI footprint. Although the SUHI effect in winter may offer certain benefits, such as alleviating cold stress and reducing heating energy consumption, summer SUHI tends to be stronger and more spatially extensive (Bartesaghi-Koc et al. 2020; Cui et al. 2021). Therefore, it remains necessary to develop adaptive mitigation strategies that account for the geographical characteristics of each city.

4.3. Usage, appalications of the suggested method

The AIA model proposed in this study contains four key parameters that can be flexibly adjusted to suit the characteristics of different cities, thereby more accurately reflecting the directional expansion and spatial distribution of the urban heat island effect:

First, the buffer size affects the spatial scale of the analysis. Smaller buffers focus more on temperature changes in the core area of the urban area, while larger buffers are more helpful in identifying the SUHI effect away from the urban area. Second, the min sector angle controls the directional resolution of the initial division. Smaller angles help identify subtle directional temperature changes, while larger angles reduce the computational complexity. Third, the max sector angle, as the upper limit of the merging process, limits whether adjacent sectors can be merged. The larger the angle, the easier it is to form a simplified SUHI footprint. Finally, the temperature threshold determines whether the temperature differences between sectors are sufficient for merging. A lower temperature threshold helps retain details, while a higher threshold emphasizes obvious temperature differences.

In addition, through q-value optimization, this method quantifies the irregular anisotropy of the SUHI effect and verifies the reliability of the division through significance testing. The adaptive and data-driven division method overcomes the limitations of fixed-angle division and provides new perspectives and methods for developing adaptive mitigation strategies that account for the geographical characteristics of each city.

4.4. Limitation and future plan

Although the AIA model effectively represents the irregular anisotropy of the SUHI footprint, it also has limitations. First, Landsat provides only daytime thermal infrared data at a spatial resolution of 30 m, which limits the ability to analyze diurnal SUHI variation and may not fully capture thermal heterogeneity in areas with complex urban morphology, such as high-density or mixed-use zones. Second, this study does not explore the potential drivers of the irregular anisotropy of the SUHI footprint, which could be addressed in future research. Additionally, the study area includes only five representative cities in Australia, and the relatively small sample size may introduce some bias, while the results also remain sensitive to parameter settings and q-value thresholds. Also, it lacks a quantitative assessment of how various intra-urban functional zones contribute to or mitigate LST, which limits the understanding of internal SUHI heterogeneity.

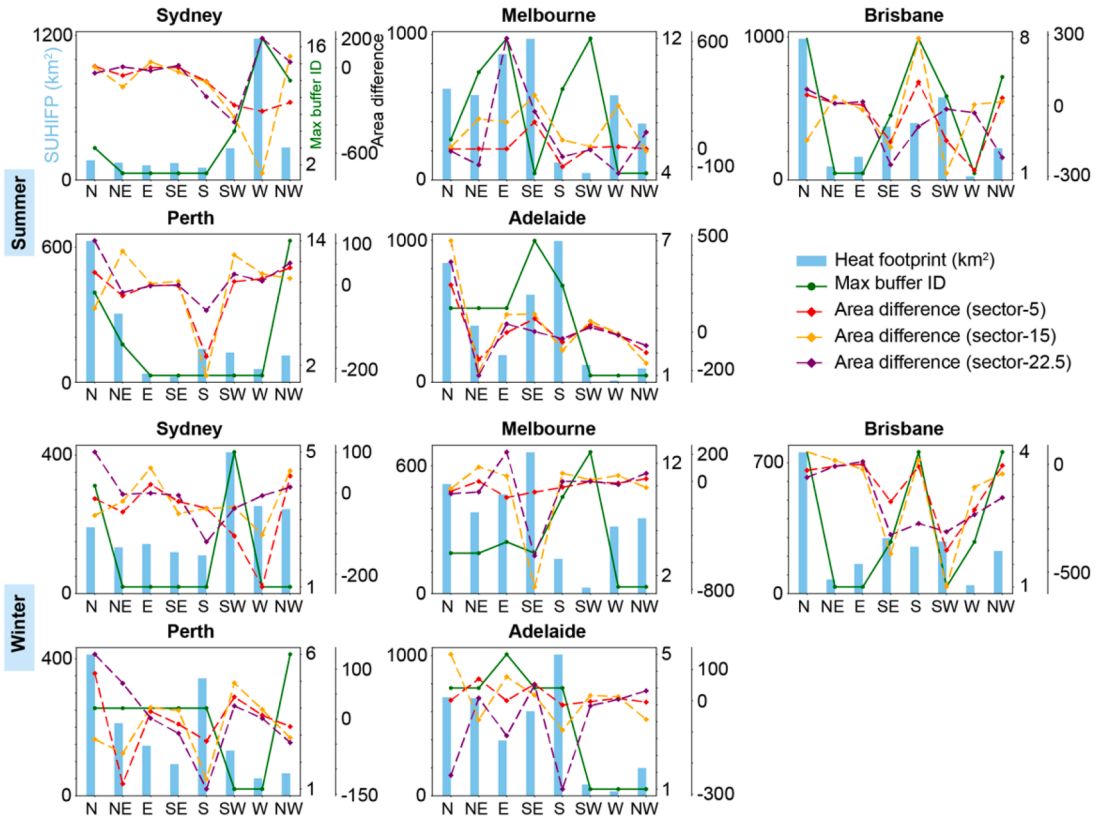

Fig. 9. Comparison of SUHI footprint anisotropy extracted by different methods.

The spatial, seasonal, and diurnal variations in SUHI intensity and footprint are important topics in urban climate research. Future research could combine MODIS with long-term diurnal and seasonal analysis of urban heat island variations, such as the rate of change of SUHI intensity in each direction, and consider the relationship between the rate of change in built-up areas and the directional variation of the SUHI footprint. Spatial heterogeneity analysis methods, such as the optimal geographic detector, could also be employed to explore the driving mechanisms behind the irregular anisotropic expansion of SUHI footprints. These analyses should consider factors such as urban morphology, land use types, and climate zones. Further exploration of the driving mechanisms of the spatial pattern of the SUHI effect can provide more meaningful insights into identifying and mitigating urban heat risks.

5. Conclusion

This study proposed an Adaptive Irregular Anisotropy (AIA) model to explore the spatial distribution and irregular anisotropy of the SUHI footprint. By dynamically adjusting temperature differences based on q-values, the model provides a clearer definition of the spatial heterogeneity of the SUHI effect.

The results show that the SUHI footprint extracted by the AIA model shows significant directional differences. In directions with a high proportion of impervious surfaces, the SUHI footprint can reach up to eight times the urban area. Specifically, Sydney's footprint is mainly concentrated on the west side in summer, Melbourne's footprint is more concentrated on the east side and relatively less on the west side, while Perth's footprint is more evenly distributed across different directions. Seasonal analysis indicates that in most cities, the footprint is larger in summer than in winter, but in Adelaide, it is more extensive in winter. Compared to other anisotropy-based footprint extraction methods, the AIA model is highly sensitive to temperature thresholds, improving q-values by 1.1 % to 44.1 %, thereby reducing footprint estimation bias to some extent and more effectively representing footprint spatial heterogeneity.

Overall, the AIA model is more suitable for areas with complex urban boundaries and mixed land use. This study highlights the importance of adaptive strategies in mitigating the SUHI effect, especially in cities with directional differences in built-up area expansion. However, the generalizability of the AIA model under different climatic conditions and urban morphologies still requires further validation. In the future, the AIA model can be extended to analyze directional variations of SUHI effects across multiple time periods or during nighttime.

CRediT authorship contribution statement

Xinyue Yang: Writing – original draft, Visualization, Methodology, Formal analysis, Data curation, Conceptualization. **Yongze Song:** Writing – review & editing, Visualization, Validation, Supervision, Methodology. **Cheolhee Yoo:** Writing – review & editing, Supervision, Methodology. **Kai Ren:** Writing – review & editing, Visualization. **Peng Wu:** Writing – review & editing, Supervision.

Declaration of competing interest

The authors declare that they have no known competing financial interests or personal relationships that could have appeared to influence the work reported in this paper.

Data availability

Data will be made available on request.

References

Alqasemi, A. S., Hereher, M. E., Kaplan, G., Al-Quraishi, A. M. F., & Saibi, H. (2021). Impact of COVID-19 lockdown upon the air quality and surface urban heat island intensity over the United Arab Emirates. *Science of the Total Environment, 767*, 11.

An, Z., Ming, Y., Liu, Y., & Zhang, G. (2025). Investigating 2D/3D factors influencing surface urban heat islands in mountainous cities using explainable machine learning. *Urban Climate, 59*, Article 102325.

Anniballe, R., & Bonafoni, S. (2015). A stable gaussian fitting procedure for the parameterization of remote sensed thermal images. *Algorithms, 8*, 82–91.

Bartesaghi-Koc, C., Osmond, P., & Peters, A. (2020). Quantifying the seasonal cooling capacity of 'green infrastructure types'(GITs): An approach to assess and mitigate surface urban heat island in Sydney, Australia. *Landscape and Urban Planning, 203*, Article 103893.

Calderón-Loor, M., Hadjikakou, M., & Bryan, B. A. (2021). High-resolution wall-to-wall land-cover mapping and land change assessment for Australia from 1985 to 2015. *Remote Sensing of Environment, 252*, Article 112148.

Chakraborty, T., Hsu, A., Manya, D., & Sheriff, G. (2020). A spatially explicit surface urban heat island database for the United States: Characterization, uncertainties, and possible applications. *ISPRS Journal of Photogrammetry and Remote Sensing, 168*, 74–88.

Clay, R., Guan, H., Wild, N., Bennett, J., & Ewenz, C. (2016). Urban heat island traverses in the city of Adelaide, South Australia. *Urban Climate, 17*, 89–101.

Cui, F., Hamdi, R., Yuan, X., He, H., Yang, T., Kuang, W., Termonia, P., & De Maeyer, P. (2021). Quantifying the response of surface urban heat island to urban greening in global north megacities. *Science of the Total Environment, 801*, Article 149553.

Das, M., Das, A., & Mandal, S. (2020). Outdoor thermal comfort in different settings of a tropical planning region: A study on Sriniketan-Santiniketan Planning Area (SSPA), Eastern India. *Sustainable Cities and Society, 63*, Article 102433.

Dialesandro, J. M., Wheeler, S. M., & Abunnasr, Y. (2019). Urban heat island behaviors in dryland regions. *Environmental Research Communications, 1*, Article 081005.

Duguay-Tetzlaff, A., Bento, V. A., Göttsche, F. M., Stöckli, R., Martins, J. P., Trigo, I., Olesen, F., Bojanowski, J. S., Da Camara, C., & Kunz, H. (2015). Meteosat land surface temperature climate data record: Achievable accuracy and potential uncertainties. *Remote Sensing, 7*, 13139–13156.

Eliades, M., Neophytides, S., Mavrovouniotis, M., Panagiotou, C. F., Anastasiadou, M. N., Varvaris, I., Papoutsa, C., Bachofer, F., Michaelides, S., & Hadjimitsis, D. (2024). Temporal Dynamics of Global Barren Areas between 2001 and 2022 Derived from MODIS Land Cover Products. *Remote Sensing, 16*, 3317.

Ermida, S. L., DaCamara, C. C., Trigo, I. F., Pires, A. C., Ghent, D., & Remedios, J. (2017). Modelling directional effects on remotely sensed land surface temperature. *Remote Sensing of Environment, 190*, 56–69.

Ermida, S. L., Soares, P., Mantas, V., Göttsche, F.-M., & Trigo, I. F. (2020). Google earth engine open-source code for land surface temperature estimation from the landsat series. *Remote Sensing, 12*, 1471.

Estoque, R. C., Murayama, Y., & Myint, S. W. (2017). Effects of landscape composition and pattern on land surface temperature: An urban heat island study in the megacities of Southeast Asia. *Science of the Total Environment, 577*, 349–359.

Gao, J., Kennedy, D. M., & McSweeney, S. (2024). Decadal changes in vegetation cover within coastal dunes at the regional scale in Victoria, SE Australia. *Journal of Environmental Management, 351*, Article 119622.

Gao, J., Meng, Q., Hu, D., Zhang, L., Hu, X., & Qian, J. (2023). A uniform methodology of local cooling and warming effects for different urban site types: multi-perspective assessment based on four northern Chinese cities. *Sustainable Cities and Society, 96*, Article 104652.

Gao, Y., Zhao, J., & Han, L. (2022). Exploring the spatial heterogeneity of urban heat island effect and its relationship to block morphology with the geographically weighted regression model. *Sustainable Cities and Society, 76*, Article 103431.

Ge, M., Fang, S., Gong, Y., Tao, P., Yang, G., & Gong, W. (2021). Understanding the correlation between landscape pattern and vertical urban volume by time-series remote sensing data: a case study of melbourne. *ISPRS International Journal of Geo-Information, 10*, 14.

Guo, A., Yang, J., Sun, W., Xiao, X., Xia Cecilia, J., Jin, C., & Li, X. (2020a). Impact of urban morphology and landscape characteristics on spatiotemporal heterogeneity of land surface temperature. *Sustainable Cities and Society, 63*, Article 102443.

Guo, A., Yang, J., Xiao, X., Xia, J., Jin, C., & Li, X. (2020b). Influences of urban spatial form on urban heat island effects at the community level in China. *Sustainable Cities and Society, 53*, Article 101972.

Harmay, N. S. M., Kim, D., & Choi, M. (2021). Urban heat island associated with land use/land cover and climate variations in Melbourne, Australia. *Sustainable Cities and Society, 69*, Article 102861.

Herath, P., Bai, X., Jin, H., & Thatcher, M. (2024). Does the spatial configuration of urban parks matter in ameliorating extreme heat? *Urban Climate, 53*, Article 101756.

Hou, H., Longyang, Q., Su, H., Zeng, R., Xu, T., & Wang, Z.-H. (2023a). Prioritizing environmental determinants of urban heat islands: A machine learning study for major cities in China. *International Journal of Applied Earth Observation and Geoinformation, 122*, Article 103411.

Hou, H., Su, H., Yao, C., & Wang, Z.-H. (2023b). Spatiotemporal patterns of the impact of surface roughness and morphology on urban heat island. *Sustainable Cities and Society, 92*, Article 104513.

Hu, L., & Brunsell, N. A. (2013). The impact of temporal aggregation of land surface temperature data for surface urban heat island (SUHI) monitoring. *Remote Sensing of Environment, 134*, 162–174.

Hu, L., & Brunsell, N. A. (2015). A new perspective to assess the urban heat island through remotely sensed atmospheric profiles. *Remote Sensing of Environment, 158*, 393–406.

Hu, L., Monaghan, A., Voogt, J. A., & Barlage, M. (2016). A first satellite-based observational assessment of urban thermal anisotropy. *Remote Sensing of Environment, 181*, 111–121.

Hu, L., & Wendel, J. (2019). Analysis of urban surface morphologic effects on diurnal thermal directional anisotropy. *ISPRS Journal of Photogrammetry and Remote Sensing, 148*, 1–12.

Hu, Y., Hou, M., Jia, G., Zhao, C., Zhen, X., & Xu, Y. (2019). Comparison of surface and canopy urban heat islands within megacities of eastern China. *ISPRS Journal of Photogrammetry and Remote Sensing, 156*, 160–168.

Huang, X., Li, L., Yan, X., Ji, W., Zhao, K., & Zhao, X. (2024). Assessment of heat exposure risk for urban populations and spatio-temporal patterns: A perspective of urban functional zones in Xi'an, China. *Urban Climate, 55*, Article 101992.

Huang, X., & Wang, Y. (2019). Investigating the effects of 3D urban morphology on the surface urban heat island effect in urban functional zones by using high-resolution remote sensing data: A case study of Wuhan, Central China. *ISPRS Journal of Photogrammetry and Remote Sensing, 152*, 119–131.

Imhoff, M. L., Zhang, P., Wolfe, R. E., & Bounoua, L. (2010). Remote sensing of the urban heat island effect across biomes in the continental USA. *Remote Sensing of Environment, 114*, 504–513.

Jamei, Y., Seyedmahmoudian, M., Jamei, E., Horan, B., Mekhilef, S., & Stojcevski, A. (2022). Investigating the relationship between land use/land cover change and land surface temperature using google earth engine; case study: Melbourne, Australia. *Sustainability, 14*, Article 14868.

Jiao, L., Dong, T., Xu, G., Zhou, Z., Liu, J., & Liu, Y. (2021). Geographic micro-process model: Understanding global urban expansion from a process-oriented view. *Computers, Environment and Urban Systems, 87*, Article 101603.

Kafy, A.-A., Bakshi, A., Saha, M., Al Faisal, A., Almulhim, A. I., Rahaman, Z. A., & Mohammad, P. (2023). Assessment and prediction of index based agricultural drought vulnerability using machine learning algorithms. *Science of the Total Environment, 867*, Article 161394.

Kim, S. W., & Brown, R. D. (2021). Urban heat island (UHI) intensity and magnitude estimations: A systematic literature review. *Science of the Total Environment, 779*, 17.

Kumar, A., Mukherjee, M., & Goswami, A. (2023). Inter-seasonal characterization and correlation of Surface Urban Heat Island (SUHI) and Canopy Urban Heat Island (CUHI) in the urbanized environment of Delhi. *Remote Sensing Applications: Society and Environment, 30*, Article 100970.

Li, D., Liao, W., Rigden, A. J., Liu, X., Wang, D., Malyshev, S., & Shevliakova, E. (2019). Urban heat island: Aerodynamics or imperviousness? *Science Advances, 5*, eaau4299.

Li, H., Zhou, Y., Jia, G., Zhao, K., & Dong, J. (2022). Quantifying the response of surface urban heat island to urbanization using the annual temperature cycle model. *Geoscience Frontiers, 13*, Article 101141.

Li, K., & Chen, Y. (2023). Identifying and characterizing frequency and maximum durations of surface urban heat and cool island across global cities. *Science of the Total Environment, 859*, Article 160218.

Li, L., Huang, X., Li, J., & Wen, D. (2017). Quantifying the spatiotemporal trends of canopy layer heat island (CLHI) and its driving factors over Wuhan, China with satellite remote sensing. *Remote Sensing, 9*, 536.

Li, L., Zhan, W., Hu, L., Chakraborty, T., Wang, Z., Fu, P., Wang, D., Liao, W., Huang, F., & Fu, H. (2023). Divergent urbanization-induced impacts on global surface urban heat island trends since 1980s. *Remote Sensing of Environment, 295*, Article 113650.

Li, X., Gong, P., Zhou, Y., Wang, J., Bai, Y., Chen, B., Hu, T., Xiao, Y., Xu, B., & Yang, J. (2020). Mapping global urban boundaries from the global artificial impervious area (GAIA) data. *Environmental Research Letters, 15*, Article 094044.

Liu, S., Zhang, J., Li, J., Li, Y., Zhang, J., & Wu, X. (2021a). Simulating and mitigating extreme urban heat island effects in a factory area based on machine learning. *Building and Environment, 202*, Article 108051.

Liu, Y., Xu, Y., Weng, F., Zhang, F., & Shu, W. (2021b). Impacts of urban spatial layout and scale on local climate: A case study in Beijing. *Sustainable Cities and Society, 68*, Article 102767.

Liu, Y., Zhang, W., Liu, W., Tan, Z., Hu, S., Ao, Z., Li, J., & Xing, H. (2024). Exploring the seasonal effects of urban morphology on land surface temperature in urban functional zones. *Sustainable Cities and Society, 103*, Article 105268.

Lu, L., Guo, H., Weng, Q., Bartesaghi-Koc, C., Osmond, P., & Li, Q. (2024). A transferable approach to assessing green infrastructure types (GITs) and their effects on surface urban heat islands with multi-source geospatial data. *Remote Sensing of Environment, 306*, Article 114119.

Marando, F., Heris, M. P., Zulian, G., Udías, A., Mentaschi, L., Chrysoulakis, N., Parastatidis, D., & Maes, J. (2022). Urban heat island mitigation by green infrastructure in European Functional Urban Areas. *Sustainable Cities and Society, 77*, Article 103564.

Nadizadeh Shorabeh, S., & Hamzeh, S. (2019). Investigating the Effects of environmental and demographic parameters on the spatial distribution of surface temperature of tehran by combining statistical and mono-window models. *Physical Geography Research, 51*, 263–282.

Naserikia, M., Hart, M. A., Nazarian, N., Bechtel, B., Lipson, M., & Nice, K. A. (2023). Land surface and air temperature dynamics: The role of urban form and seasonality. *Science of the Total Environment, 905*, Article 167306.

Oh, J. W., Ngarambe, J., Duhirwe, P. N., Yun, G. Y., & Santamouris, M. (2020). Using deep-learning to forecast the magnitude and characteristics of urban heat island in Seoul Korea. *Scientific Reports, 10*, 3559.

Oukawa, G. Y., Krecl, P., & Targino, A. C. (2022). Fine-scale modeling of the urban heat island: A comparison of multiple linear regression and random forest approaches. *Science of the Total Environment, 815*, Article 152836.

Peng, J., Xie, P., Liu, Y., & Ma, J. (2016). Urban thermal environment dynamics and associated landscape pattern factors: A case study in the Beijing metropolitan region. *Remote Sensing of Environment, 173*, 145–155.

Pfautsch, S., Wujeska-Klause, A., & Walters, J. R. (2024). Spatiotemporal variation of intra-urban heat and heatwaves across Greater Sydney, Australia. *Weather and Climate Extremes*, Article 100741.
Qiao, Z., Wu, C., Zhao, D., Xu, X., Yang, J., Feng, L., Sun, Z., & Liu, L. (2019). Determining the boundary and probability of surface urban heat island footprint based on a logistic model. *Remote Sensing, 11*, 1368.
Qin, B., Cao, B., Roujean, J.-L., Gastellu-Etchegorry, J.-P., Ermida, S. L., Bian, Z., Du, Y., Hu, T., Li, H., & Xiao, Q. (2023). A thermal radiation directionality correction method for the surface upward longwave radiation of geostationary satellite based on a time-evolving kernel-driven model. *Remote Sensing of Environment, 294*, Article 113599.
Quan, J., Chen, Y., Zhan, W., Wang, J., Voogt, J., & Wang, M. (2014). Multi-temporal trajectory of the urban heat island centroid in Beijing, China based on a Gaussian volume model. *Remote Sensing of Environment, 149*, 33–46.
Rehman, A., Radulescu, M., Ma, H., Dagar, V., Hussain, I., & Khan, M. K. (2021). The impact of globalization, energy use, and trade on ecological footprint in Pakistan: Does environmental sustainability exist? *Energies, 14*, 5234.
Renard, F., Alonso, L., Fitts, Y., Hadjiosif, A., & Comby, J. (2019). Evaluation of the effect of urban redevelopment on surface urban heat islands. *Remote Sensing, 11*, 299.
Schwarz, N., Schlink, U., Franck, U., & Großmann, K. (2012). Relationship of land surface and air temperatures and its implications for quantifying urban heat island indicators—An application for the city of Leipzig (Germany). *Ecological Indicators, 18*, 693–704.
Shao, L., Liao, W., Li, P., Luo, M., Xiong, X., & Liu, X. (2023). Drivers of global surface urban heat islands: Surface property, climate background, and 2D/3D urban morphologies. *Building and Environment, 242*, Article 110581.
Sharifi, E., Larbi, M., Omrany, H., & Boland, J. (2020). Climate change adaptation and carbon emissions in green urban spaces: Case study of Adelaide. *Journal of Cleaner Production, 254*, Article 120035.
Sharmin, T., Chappell, A., & Lannon, S. (2024). Spatio-temporal analysis of LST, NDVI and SUHI in a coastal temperate city using local climate zone. *Energy and Built Environment*.
Shi, L., Ling, F., Foody, G. M., Yang, Z., Liu, X., & Du, Y. (2021). Seasonal SUHI analysis using local climate zone classification: A case study of Wuhan, China. *International Journal of Environmental Research and Public Health, 18*, 7242.
Shi, S., Ji, S., & Luo, Z. (2025). Spatial heterogeneity, interaction and multi-scale effects of driving factors of heat island intensity in different urban agglomerations. *Sustainable Cities and Society*, Article 106401.
Simwanda, M., Ranagalage, M., Estoque, R. C., & Murayama, Y. (2019). Spatial analysis of surface urban heat islands in four rapidly growing African cities. *Remote Sensing, 11*, 20.
Song, Y., Wang, J., Ge, Y., & Xu, C. (2020). An optimal parameters-based geographical detector model enhances geographic characteristics of explanatory variables for spatial heterogeneity analysis: Cases with different types of spatial data. *GIScience & Remote Sensing, 57*, 593–610.
Song, Y., & Wu, P. (2021). An interactive detector for spatial associations. *International Journal of Geographical Information Science, 35*, 1676–1701.
Taha, H. (1997). Urban climates and heat islands: albedo, evapotranspiration, and anthropogenic heat. *Energy and Buildings, 25*, 99–103.
Tanoori, G., Soltani, A., & Modiri, A. (2024). Machine learning for urban heat island (UHI) analysis: Predicting land surface temperature (LST) in urban environments. *Urban Climate, 55*, Article 101962.
Tao, F., Hu, Y., Tang, G., & Zhou, T. (2021). Long-term evolution of the SUHI footprint and urban expansion based on a temperature attenuation curve in the Yangtze River Delta Urban Agglomeration. *Sustainability, 13*, 8530.
Unal Cilek, M., & Cilek, A. (2021). Analyses of land surface temperature (LST) variability among local climate zones (LCZs) comparing Landsat-8 and ENVI-met model data. *Sustainable Cities and Society, 69*, Article 102877.
Voelkel, J., Hellman, D., Sakuma, R., & Shandas, V. (2018). Assessing vulnerability to urban heat: A study of disproportionate heat exposure and access to refuge by socio-demographic status in Portland, Oregon. *International Journal of Environmental Research and Public Health, 15*, 640.
Voogt, J. A., & Oke, T. R. (2003). Thermal remote sensing of urban climates. *Remote Sensing of Environment, 86*, 370–384.
Wang, H., Yi, T., Lu, Y., Wang, Y., & Wu, J. (2025). Patterns of nighttime surface urban heat island patch in mega urban agglomerations: a case study in the Pearl River Delta, China. *Sustainable Cities and Society, 128*, Article 106465.
Wang, J.-F., Zhang, T.-L., & Fu, B.-J. (2016). A measure of spatial stratified heterogeneity. *Ecological indicators, 67*, 250–256.
Wang, Y., Wang, H., Yao, F., Stouffs, R., & Wu, J. (2024). An integrated framework for jointly assessing spatiotemporal dynamics of surface urban heat island intensity and footprint: China, 2003–2020. *Sustainable Cities and Society, 112*, Article 105601.
Wu, W., & Chen, R. (2024). Finding Oasis Cold Island Footprints Based on a Logistic Model—A Case Study in the Ejina Oasis. *Remote Sensing, 16*, 2895.
Xie, J., Zhou, S., Chung, L. C. H., & Chan, T. O. (2024). Evaluating land-surface warming and cooling environments across urban–rural local climate zone gradients in subtropical megacities. *Building and Environment, 251*, Article 111232.
Xu, D., Wang, Y., Zhou, D., Wang, Y., Zhang, Q., & Yang, Y. (2024a). Influences of urban spatial factors on surface urban heat island effect and its spatial heterogeneity: A case study of Xi'an. *Building and Environment, 248*, Article 111072.
Xu, H., Li, C., Hu, Y., Wang, H., Wen, D., Li, Z., Ping, X., Wang, Q., & Li, Q. (2024b). Spatiotemporal evolution and influencing factors of surface urban heat island footprint across different-sized cities. *Urban Climate, 54*, Article 101852.
Yang, K., Tao, F., Wang, C. L., Wang, Z. L., Han, Q. L., & Zhou, T. (2023a). An optimization method for surface urban heat island footprint extraction based on anisotropy assumption. *Urban Climate, 49*, 14.
Yang, K., Zhou, T., Wang, C., Wang, Z., Han, Q., & Tao, F. (2022). RSEDM: A new rotational-scan exponential decay model for extracting the surface urban heat Island Footprint. *In, Remote Sensing*.
Yang, M., Ren, C., Wang, H., Wang, J., Feng, Z., Kumar, P., Haghighat, F., & Cao, S.-J. (2024). Mitigating urban heat island through neighboring rural land cover. *Nature Cities, 1*, 522–532.
Yang, Q., Huang, X., & Tang, Q. (2019). The footprint of urban heat island effect in 302 Chinese cities: Temporal trends and associated factors. *Science of the Total Environment, 655*, 652–662.
Yang, Q. Q., Xu, Y., Tong, X. H., Huang, X., Liu, Y., Chakraborty, T., Xiao, C. J., & Hu, T. (2023b). An adaptive synchronous extraction (ASE) method for estimating intensity and footprint of surface urban heat islands: A case study of 254 North American cities. *Remote Sensing of Environment, 297*, 20.
Yao, L., Sun, S., Song, C., Li, J., Xu, W., & Xu, Y. (2021). Understanding the spatiotemporal pattern of the urban heat island footprint in the context of urbanization, a case study in Beijing, China. *Applied Geography, 133*, Article 102496.
Yelixiati, H., Tong, L., Luo, S., & Chen, Z. (2024). Spatiotemporal heterogeneity of the relationship between urban morphology and land surface temperature at a block scale. *Sustainable Cities and Society, 113*, Article 105711.
Yu, H., & Sun, D. (2024). Quantification of Urban Heat Island Effect and Differences in Regional Influence Based on Footprint Analysis: A Case Study of the Beijing–Tianjin–Hebei Urban Agglomeration. *IEEE Journal of Selected Topics in Applied Earth Observations and Remote Sensing, 17*, 6910–6919.
Zhang, A. Q., & Xia, C. (2024). A new two-step estimation approach for retrieving surface urban heat island intensity and footprint based on urban-rural temperature gradients. *International Journal of Geographical Information Science, 38*, 2348–2378.
Zhong, S., Wang, M., Zhu, Y., Chen, Z., & Huang, X. (2022). Urban expansion and the urban–rural income gap: Empirical evidence from China. *Cities (London, England), 129*, Article 103831.
Zhou, D., Sun, S., Li, Y., Zhang, L., & Huang, L. (2023). A multi-perspective study of atmospheric urban heat island effect in China based on national meteorological observations: Facts and uncertainties. *Science of the Total Environment, 854*, Article 158638.
Zhou, D., Zhao, S., Zhang, L., Sun, G., & Liu, Y. (2015a). The footprint of urban heat island effect in China. *Scientific Reports, 5*, Article 11160.
Zhou, D. C., Zhao, S. Q., Liu, S. G., Zhang, L. X., & Zhu, C. (2014). Surface urban heat island in China's 32 major cities: Spatial patterns and drivers. *Remote Sensing of Environment, 152*, 51–61.
Zhou, D. C., Zhao, S. Q., Zhang, L. X., Sun, G., & Liu, Y. Q. (2015b). The footprint of urban heat island effect in China. *Scientific Reports, 5*, 11.
Zhu, S., Yan, Y., Zhao, B., & Wang, H. (2025). Assessing the impact of adjacent urban morphology on street temperature: A multisource analysis using random forest and SHAP. *Building and Environment, 267*, Article 112326.